

3D SIMULATIONS AND MLT: II. RA-ILES RESULTS

W. DAVID ARNETT¹, CASEY MEAKIN^{1,2}, RAPHAEL HIRSCH^{3,4}, ANDREA CRISTINI^{3,7}, CYRIL GEORGY⁵,
SIMON CAMPBELL⁶, LAURA J. A. SCOTT³, AND ETIENNE A. KAISER³

¹Steward Observatory, University of Arizona, 933 N. Cherry Avenue, Tucson AZ 85721

²Karagozian & Case, Inc., Glendale, CA 91203

³Astrophysics Group, Keele University, Lennard-Jones Laboratories, Keele, ST5 5BG, UK

⁴Kavli IPMU (WPI), The University of Tokyo, Kashiwa, Chiba 277 8583, Japan

⁵Department of Astronomy, University of Geneva, Ch. Maillettes 51, 1290 Versoix, Switzerland

⁶Monash Centre for Astrophysics, School of Physics and Astronomy, Monash University, Clayton, Australia 3800

⁷Department of Physics and Astronomy, University of Oklahoma, Norman OK 73019

ABSTRACT

In a previous paper (Arnett, et al 2019, paper I) we introduced the use of Reynolds averaged implicit large eddy simulations (RA-ILES; Mocák, et al. 2018) to the classical problem of stellar convection (Böhm-Vitense 1958). We explored the structure of turbulent boundary layers, multi-modal behavior, intermittency, fluctuations, and composition gradients, and found that the Kolmogorov dissipation length played a role in some respects akin to the Böhm-Vitense mixing length. We now extend our analysis by extracting the sub-grid dissipation of our method (the “mixing length”), and by quantifying errors in resolution of boundary layers. The results for weakly-stratified convection show quantitative agreement with the four-fifths law of Kolmogorov. We examine the differences between weakly and strongly stratified convection (i.e., core convection and surface convection zones, respectively). We find that MLT is a weak-stratification theory (which ignores turbulent kinetic energy), and for precise work *should be modified for strong-stratification cases like the solar and stellar atmospheres*. We derive the ‘effective mixing length’ for strong-stratification; it is the *density* scale height, so $\alpha \approx \Gamma \sim 5/3$, in surprising agreement with many stellar evolution calibrations, but smaller than the preferred values for the Standard Solar Model (e.g., Vinyoles, et al. 2017, SSM), an error we attribute in part to the lack of a turbulent boundary layer, which we find at the bottom of the convection zone but missing in MLT and SSM.

1. INTRODUCTION

The two main sites of convection in stars are (1) thermonuclear burning zones, and (2)

stellar atmospheres. The former occur in the hottest regions (the cores), where density gradients are small, the latter in the coolest regions (the envelopes), where density gradients are large. The simpler case, weak stratification, is relevant to burning regions and core convection. Strong stratification modifies con-

Corresponding author: wdarnett@gmail.com

vection in modest but important ways, and is appropriate to surface convection zones.

In §2 we summarize results from (Arnett, et al 2019, paper I) to provide a conceptual background for the transition from MLT conventions to three-dimensional simulations (321D). In §3 we quantify the sub-grid dissipation of our ILES simulations. In §4 we examine the case of weak stratification and in §5 the case of strong stratification. In §6 we present our conclusions.

2. SOME INSIGHTS FROM THE TURBULENT KINETIC ENERGY EQUATION

The 3D simulations of turbulence have a very large number of degrees of freedom; to understand them we proceed in stages: (1) the direct ILES numerical results, (2) Reynolds-average (RA) analysis, (3) approximate analytic solutions which track the more complex results, but with a much reduced set of degrees of freedom. The latter provide a easier comparison to MLT, which we will exploit. This reduction parallels the method of Holmes, Lumley & Berkooz (1996) in spirit, but in contrast we use Reynolds averaged implicit large eddy simulations (RA-ILES) to identify dominant terms (Viallet, et al. 2013). Here we summarize some results (Arnett, et al 2019) for convenience in discussion.

2.1. Length scale for convective velocity

Baryon conservation and the assumption of a quasi-static, quasi-spherical background place strong general constraints on the nature of convective flow in stars: mass flux balance

$$\nabla \cdot \rho \mathbf{v} = 0 \quad (1)$$

implies, for a spherically symmetric star,

$$\nabla \cdot \mathbf{v} = v_r / H_\rho, \quad (2)$$

where H_ρ is the density scale height¹ defined as $-(\partial \ln \rho / \partial r)^{-1}$. For upflow, $v_r > 0$, so the matter expands (divergence is positive), and for downflows, $v_r < 0$, and it compresses. For finite H_ρ (nonzero stratification), baryon conservation requires that the downflows, which have lower entropy and enter regions of increased pressure, are faster, narrower and denser on average than the upflows, breaking the up-down symmetry of the flow.

Eq. 2 connects the convective velocity structure to a length scale without any MLT assumption. For a medium of uniform density, $H_\rho \rightarrow \infty$, and the scale becomes the size of the turbulent medium (the convection zone), Δ_{cz} , which is finite. Thus $\ell \sim \min[\Delta_{cz}, H_\rho]$. This does give the characteristic *length scale* for a quasi-steady flow in a stratified medium (such as stellar convection). However, this equation is linear in velocity, so that the velocity scale is not constrained; another equation is required (involving the turbulent acceleration, or the turbulent kinetic energy for example). Lorenz (1963) showed that the simplest case of such flows, a 2D convective roll, is an example of deterministic chaos.² Such instabilities are associated with one or several strange attractors, and act as seeds for turbulence (Arnett, et al 2019, paper I).

2.2. Length scale for turbulent damping

Stellar Reynolds numbers³ are far larger than we encounter terrestrially (Arnett & Meakin 2016), making stellar flows highly turbulent. Kolmogorov (1962, 1941) showed that ϵ_K , the rate of flow of turbulent specific kinetic

¹ A related length, the *pressure* scale height is usually used in MLT, where $H_P = -(\partial \ln P / \partial r)^{-1}$.

² See Arnett & Meakin (2011) for a roll model, and also Gabriel & Belkacem (2018) for a plume model.

³ The Reynolds number is the product of macroscopic scales of length and velocity, divided by the viscosity, a microscopic quantity (Landau & Lifshitz 1959, Eq. 19.1).

energy through a 3D turbulent cascade, is determined by the large scale flows (Landau & Lifshitz (1959), §31),

$$\epsilon_K = \overline{v^3}/\ell_d, \quad (3)$$

where v is the speed and $\ell_d = \alpha H_P$ the linear size of such flows. The flows at these large scales are affected by boundary conditions, so that α is not a universal constant, but may depend upon the flow considered. Eq. 3 may apply only on average (Arnett, Meakin & Young 2009), and would correspond (Arnett, et al. 2015) to a drag (negative acceleration) of

$$\mathcal{D} = -\mathbf{v}|v|/\ell_d. \quad (4)$$

2.3. Turbulent kinetic energy

The chaotic driving of turbulence causes large fluctuations, and requires that we average instantaneous properties to obtain useful variables for stellar evolution (§2.6 in Arnett, et al. (2015), and Meakin & Arnett (2007b)). We do a double average, over angles (spherical shells), and over several turnover times (e.g., Tables 1, 2, 3),

$$\tau_{\text{to}} = 2\Delta r_{cz}/v, \quad (5)$$

which are short compared to evolutionary times⁴. Here v is a typical speed and Δr_{cz} is the depth of the convection zone.

For weakly-stratified convection zones (and MLT) the driving is done by buoyancy alone (the work done by buoyant acceleration \mathcal{B} acting on the turbulent velocity \mathbf{v}), so

$$\overline{\mathbf{v} \cdot \mathcal{B}} = \overline{\mathbf{v} \cdot \mathbf{g} \beta_T \Delta \nabla}, \quad (6)$$

where the gravitational acceleration vector is \mathbf{g} , the super-adiabatic excess is $\Delta \nabla = \nabla - \nabla_e$,

⁴ For hydrogen and helium burning the turnover time τ_{to} is so much shorter than the nuclear burning times that the convective algorithm may be “stiff” (Acton 1970), and require special attention. For later burning stages the times scales become shorter, and ease this problem.

and β_T is the thermal expansion coefficient (Kippenhahn & Weigert 1990). The entropy excess $\Delta \nabla$ may contain contributions from composition differences, which are ignored in MLT. To evaluate these, the issue of mixing must be solved consistently with that of convection, complicating the problem (Arnett, et al. 2015; Woodward et al. 2015; Mocák, et al. 2018).

The rate of dissipation of turbulent kinetic energy due to the turbulent cascade is, on average,

$$\overline{\mathbf{v} \cdot \mathcal{D}} \approx \epsilon_K, \quad (7)$$

which, for homogeneous isotropic turbulence, is the Kolmogorov value (Kolmogorov 1962); see §4.2 below.

We may write a turbulent kinetic energy equation (Meakin & Arnett 2007b; Arnett, et al 2019),

$$d(v^2/2)/dt = \mathbf{v} \cdot \mathcal{B} - \mathbf{v} \cdot \mathcal{D}, \quad (8)$$

for which the steady-state solution⁵ is a balance between driving and damping.

For MLT we have $\ell_d \equiv \ell_{MLT}^2/8H_P$, and $\Delta \nabla > 0$. However in Eq. 8, negative values of $\Delta \nabla$ can be allowed; this permits buoyant deceleration.

The flow is relative to the grid of the background stellar evolution model, so the co-moving time derivative of turbulent kinetic energy may also be written as

$$d(v^2/2)/dt = \partial_t(\mathbf{v} \cdot \mathbf{v})/2 + \nabla \cdot \mathbf{F}_K, \quad (9)$$

where $\mathbf{F}_K = \rho \mathbf{v}(\mathbf{v} \cdot \mathbf{v})/2$ is a flux of turbulent kinetic energy. This flux acts to spread locally-driven turbulence more evenly over the turbulent region, to be dissipated as Kolmogorov suggested. Eq. 8 and 9 together comprise a spartan form of the turbulent kinetic energy equation, when the variables are understood

⁵ Care must be taken (for negative v) with the sign of the ‘transit time’ $\tau = \tau_{\text{to}}/2$ and the deceleration.

to be properly averaged over time and angle (Meakin & Arnett 2007b).

2.4. Local balance

When performed on even modestly resolved numerical simulations of weakly stratified convective shell burning (a few pressure scale heights), such averaging shows a balance over the turbulent region, between (1) large scale driving by buoyancy and (2) dissipation at the small-scale end of the turbulent cascade. Convection in strong stratification ($\Delta r_{cz} \gg 2H_P$) is also driven by “pressure dilatation” as well as buoyancy (Viallet, et al. 2013); an issue to which we will return (§5).

Our RA-ILES numerical simulations for weakly-stratified convection satisfy a local balance between buoyancy and turbulent drag, on average, so

$$\bar{B} \approx \bar{D}, \quad (10)$$

(Meakin & Arnett 2007b; Arnett, et al. 2015). In a quasi-steady state for a weakly-stratified convection zone, the divergence of the turbulent kinetic energy flux, $\nabla \cdot \mathbf{F}_K$, is small (upflows mostly cancel downflows). However pulses are caused by phase lags which occur between driving and damping. Thus, on average,

$$v^2/\ell_d \approx g\beta_T\Delta\nabla, \quad (11)$$

which is something like MLT, e.g., (Kippenhahn & Weigert 1990, Eq. 7.6). This equation is nonlinear in velocity and therefore can set a velocity scale for Eq. 2, but *with the Kolmogorov damping length ℓ_d replacing the mixing length*.

2.5. Singularities

As Eq. 11 implies, there are obvious mathematical problems in MLT: (1) the turbulent speed v is imaginary for $\Delta\nabla$ negative, and (2) behavior within a distance ℓ_d of a boundary is

undefined. The simulations⁶ support a more general equation for turbulent kinetic energy, Eq. 8, which suggests answers to these problems (Arnett, et al 2019, paper I). The singularities in MLT at the convective zone boundaries (§9 in Gough 1977), and in boundary layers (§40 in Landau & Lifshitz 1959) can be removed by the introduction of the total time derivative of the specific turbulent kinetic energy.

The singularities in the boundary layers occur in Prandtl’s equations as the velocity perpendicular to the surface goes to zero. In a star the motion does not go to zero but becomes wave-like rather than turbulent (Meakin & Arnett 2007b). If the Mach numbers are low, as they usually are in stellar interiors, gravity (g -)modes dominate over compressional (p -)modes.

In MLT, a cut is made at $v = 0$ to match convective and non-convective regions, removing the imaginary velocity at $\Delta\nabla < 0$ in Eq. 11. This join is not done correctly in a dynamic sense, as a finite convective velocity jumps to zero as the cut is crossed, requiring infinite acceleration (Renzini’s “ends problem”, Arnett, et al 2019).

A related issue is the behavior of the velocity field beyond, but in the vicinity of, the boundary. (Arnett, et al. 2015) have shown that use of the spatial derivatives (Eq. 9) allows continuation through the singularity at the cut. Use of the partial derivatives with respect to time, i.e., wave motion, also can avoid the singularity, at the expense of allowing for entrainment and wave generation.

In MLT, Eq. 11 implies mixing if $\Delta\nabla > 0$. Simulations show rapid mixing, so that this becomes the Schwarzschild (not Ledoux) criterion for convective instability. At the boundary a deceleration and turning of the flow oc-

⁶ See also Meakin & Arnett (2007b).

curs by negative buoyancy $\Delta\nabla < 0$ in a well-mixed braking zone, and the Richardson criterion becomes relevant (Arnett, et al. 2015) between the well-mixed convection zone and the poorly mixed neighboring region (Turner 1973; Arnett, et al 2019).

3. SUB-GRID DISSIPATION

A feature of ILES, not easily reproduced for stellar parameters in direct numerical simulation (DNS), is the automatic development of a Kolmogorov cascade, allowing a description of large scale flows down into the inertial range. See (Porter & Woodward 2000, Fig. 4), (Cristini, et al. 2017, Fig. 8), and (Radice, Couch & Ott 2015, Fig. 5), for examples of specific turbulent kinetic energy spectra.

3.1. The O+O shell subgrid dissipation

Using RA-ILES we construct our Fig. 1, which shows the time-averaged sub-grid dissipation (weighted by mass per unit length) for the oxygen burning shell, versus radius. *We find that the sub-grid dissipation due to turbulent cascade (the “hill” in Fig. 1, between $r \sim 0.43$ and 0.85×10^9 cm) is not sensitive to zoning, from 128^3 to 1536^3 , and has a Kolmogorov value over the averaging window in time.* See also §4 below. Errors due to low resolution in the lower boundary are easily seen, which begin to disappear with finer resolution. The dissipation in the upper boundary showed signs of a similar “spike” at very crude zoning but converged within the range of resolutions shown in the figure. This milder condition for numerical convergence on the upper boundary is expected because of the larger scale heights in all of the structural and flow fields there. For more extensive discussion, see Arnett, et al. (2015); Cristini, et al. (2017, 2018); Grinstein, Magolin & Rider (2007), and the article by Woodward (2007) in particular.

If we imagine sufficient computer power and time, the problem could be resolved down to

the physical dissipation scale, as in a DNS calculation, in which the “hill” would disappear at some resolution (the physical Kolmogorov scale) which depends upon the physical viscosity. This is vastly unfeasible at present, so that the “hill” corresponds to the flux of energy in the turbulent cascade, going to the sub-grid scales. In ILES the “hill” never disappears because the dissipation is always numerical, occurring at the numerical “Kolmogorov scale”, and is pushed to smaller scales with more refined zoning. The numerical “Kolmogorov scale” is essentially the grid scale.

The “hill” shows a mild multi-modal fluctuation (see §5, Arnett, et al (2019)), despite being averaged over a few turnover times. *The necessity to average, over many ($\gg 4$) turnover times, makes the determination of accurate time behavior expensive for the highest space resolutions.* Unlike the stable regions ($r < 0.43 \times 10^9$ cm and $r > 0.85 \times 10^9$ cm), which have solutions that are attracted to a constant curve, the convective region has fluid trajectories which diverge with time⁷, so that they are attracted to a limit curve in an average sense, *but with fluctuations around that limit curve.* This resembles the behavior of the Lorenz model with its strange attractor (Arnett & Meakin 2011), *which also is never “static” except when averaged over many cycles.* Fig. 1 in Arnett, et al (2019) and the corresponding movies show interactions of multiple 3D convective rolls (each of which is a more general version of the Lorenz 2D roll).

3.2. The C+C shell subgrid dissipation

Figure 2 shows the time-averaged sub-grid dissipation for the carbon burning shell as a function of radius (weighted by mass per unit length). Unlike Fig. 1, there is no ingestion of a new and different fuel (^{20}Ne); so the evolu-

⁷ See Lyapunov exponent discussion in §5.2.4 of Manneville (2010).

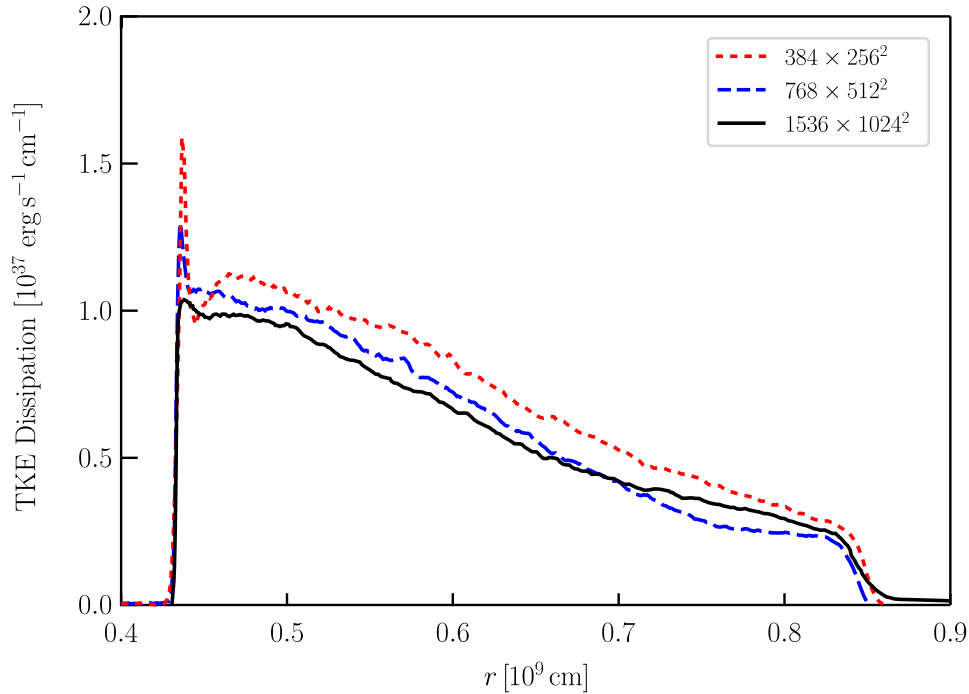


Figure 1. Time-averaged sub-grid dissipation for the oxygen burning shell, versus radius. This shows the “med-res” (384×256^2 , dots) and “hi-res” cases (768×512^2 , heavy dots) of (Viallet, et al. 2013), and a “very-hi-res” case (1536×1024^2 , heavier dots) (the “Perth” simulation, see Arnett, et al. (2015)). The “spike” at $r \sim 0.43 \times 10^9$ cm is due to poor resolution of the lower (thinner) boundary layer, and begins to vanish at the highest resolution. The upper boundary layer seems well resolved in space, but pulses in time. The remaining dissipation (the “hill” between $r \sim 0.44 \times 10^9$ cm and $r \sim 0.85 \times 10^9$ cm), which is statistically steady but not static, is due to damping of turbulence at the smallest (sub-grid) scales, and is found to be consistent *on average* with Kolmogorov theory (see text). Ingestion of ^{20}Ne also causes heating and evolution of the background (Mocák, et al. 2018); this is absent in the C+C shell (Fig. 2). The number of turnovers taken to construct the curves is limited by computational cost; med-res, hi-res and very hi-res have 4, 2.1 and < 2 turnovers.

tion is smoother (see [Mocák, et al. \(2018\)](#) for further discussion of ^{20}Ne ingestion in Fig. 1). Here we have (4.0, 4.4, 10.6, 1.5) turnovers for zoning of (128^3 , 256^3 , 512^3 , 1024^3), so the highest resolution in space corresponds to the poorest statistics in time because of the need to disentangle the chaotic, multi-mode behavior. Despite this, there is a tendency toward convergence, but modulated by multi-mode variations, which cancel less well for fewer turnovers. The solutions are chaotic, with each new resolution resetting the initial conditions, so that the solutions converge to a manifold of curves with the same average properties (like the Lorenz roll), not a single curve.

[Holmes, Lumley & Berkooz \(1996\)](#) (see their Chapter 3) suggest the importance of low order modes and the application of proper orthogonal decomposition (POD) to the energy-containing scales of turbulence. In our simulations, most of the turbulent kinetic energy is indeed contained in a few low order modes⁸ of moderately large scale, consistent with the Kolmogorov cascade, although there are many more modes with relatively little energy.

3.3. Resolution

Grid resolution in space is associated with the “spikes” at the boundary layers, which can be made smaller with the finer zoning. Determination of the behavior in time is complicated by association with the chaotic fluctuations of larger scale coherent structures that make up the “hill”. The time resolution is set by the Courant condition (minimum sound travel time across a zone), which is adequately small, but the mixed modes require longer time sequences (more turnover times) to disentangle.

⁸ For the O+O shell, the lowest POD mode has ~ 45 percent of the turbulent energy, with ~ 75 percent in lowest 4 modes, during the 400 s examined by [Meakin & Arnett \(2007b\)](#). For the C+C shell, which has no significant ingestion of a new fuel, the flow is simpler, and the lowest 3 modes dominate.

gle. There is no indication as yet that the long term behavior can not be accurately determined from simulations of longer duration.

Figures 1 and 2 provide insight into the zoning required to spatially resolve the thin lower boundary layer. The “Perth” simulation of the O+O shell, at 1536×1024^2 , seems already to be reducing the “spike” into a merger with the “hill”, although the turnover statistics are poor for the short duration in time (see Table 1).

It appears that the dissipation rate in the “spikes” in Fig. 1 (and 2) may be converging to a small value with higher resolution. The composition profiles may also converge to a fixed shape ([Cristini, et al. 2018](#), their Fig. 16.). This must be due to numerical dissipation, but *a numerical dissipation which is constrained by the ILES sub-grid model, as is the turbulent cascade*. A turbulent boundary layer develops between convection and non-convective regions, which ILES seems to represent robustly. Such an explanation may be tested by future simulations, at higher resolution.

A related problem is that of the resolution of entrainment ([Meakin & Arnett 2007b](#); [Cristini, et al. 2017](#)), which also involves the turbulent boundary layer. [Woodward et al. \(2015\)](#) have shown that the entrainment rate in a simulation depends upon the zoning, and with due caution, suggest that their 1536^3 may already capture the Kelvin-Helmholtz waves (which they and we believe drive the entrainment). This seems consistent with our “Perth” simulation, which does not have the advantage of “PPB advection” ([Woodward et al. 2015](#)), but does have the improved brute-force resolution of “box-in-star” gridding ([Arnett, et al. 2015](#)). The effects of the differing boundary conditions (a sector versus 4π steradians) remains to be explored fully.

Now that we better understand simulations of the turbulent cascade and coherent structures on a fixed grid, we have a basis for valida-

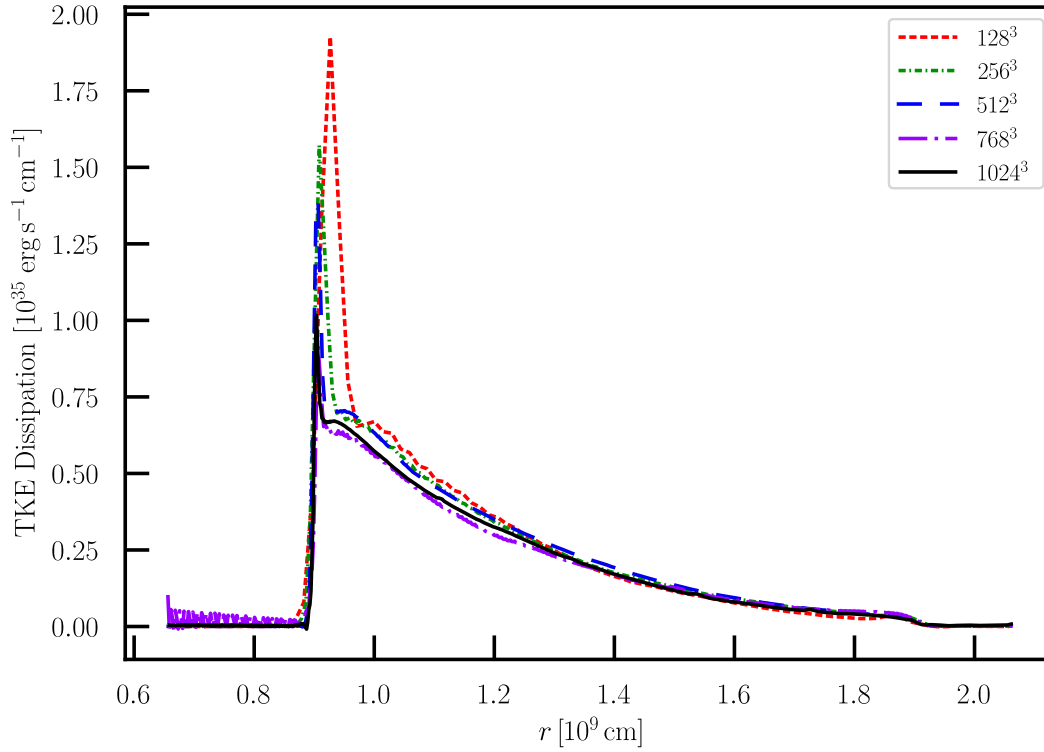


Figure 2. Time-averaged sub-grid dissipation for the carbon burning shell, versus radius. This shows the 128^3 , 256^3 , 512^3 , 768^3 , and 1024^3 cases of (Cristini, et al. 2017, 2018). The 1536^3 case is not shown because an inadequate number (< 1) of turnover times were available for a robust time average. Unlike the O+O simulation, the simpler burning associated with C+C has no strong ingestion of new fuel, but the effect of finer zoning seems similar. The “spike” monotonically decreases in size with increased zoning, and the “hill” settles toward an asymptotic shape and size.

tion tests for possible further speedup of such simulations. For example, do we need to resolve down to the inertial range over the whole convection zone? In the same vein, Radice, Couch & Ott (2015) report experience with the FLASH code that some higher-order Riemann solvers give deeper penetration into the inertial range for the same computational cost. Finally, adapting simulation codes to better utilize newer hardware (e.g., GPU’s) is desirable. Computational efficiency is a multi-parameter problem, involving the code (PROMPI scales well), the algorithm (PPB increases accuracy), microphysics algorithms (equation of state and reaction networks), the compiler, the computer architecture, and so on, all of which should be tuned to the problem at hand. Indications that the problem is close to being resolved make the issue more acute.

4. TURBULENT DISSIPATION LENGTH FOR WEAK STRATIFICATION

Joyce & Chaboyer (2018) suggest that it is no longer acceptable for precise stellar models to use solar-calibrations of the mixing-length, and advocate implementation of “an adaptive mixing-length” to maintain fidelity with high precision observations.

Which mixing-length? In §2.3 we saw that the Kolmogorov dissipation length may behave like a mixing length to some extent. It may be instructive to construct such a “mixing-length” ℓ from a 3D simulation, in order to clarify the physics involved (and missing). However, the details of boundaries, formulation of MLT, averaging domains in time and in space for simulations, chaotic fluctuations driven by strange attractors, inadequacies in the simulations, and variation in initial models, all introduce inconsistencies. MLT uses $\alpha = \ell/H_P$ in multiple ways, further confusing the comparison of stellar models to sim-

ulations.⁹ Much of the variance seems to be due to choices of how to project the complex 3D data set onto a 1D MLT framework which is physically incomplete; in contrast high resolution ILES gives reasonably consistent results for the dissipation rate ϵ_K , (Porter & Woodward 2000; Meakin & Arnett 2007b; Arnett, et al. 2015; Jones, et al., 2017; Cristini, et al. 2017).

4.1. Resolution, geometry and sampling

We emphasize that both the dissipation rate ϵ_K and the rms velocity v_{rms} vary as the turbulent kinetic energy varies (Meakin & Arnett (2007b); Cristini, et al. (2017); Arnett, et al (2019)), so that ℓ is constant only if averaged. Such averaging is required for robust results.

Arnett & Meakin (2011) have discussed some of the issues involved in averaging over fluctuating turbulent cells. For a steady-state distribution, a “snapshot average” over a large volume and short time should give the same value as an “accumulation average” in a small volume over a long time. For stellar evolution the averaging must be able to smooth the “shot noise” of individual turbulent events. Arnett, et al (2019) presented fly-through and evolutionary movies which suggest both approaches are feasible, after a steady state is attained.

Two limiting cases are plane and spherical geometry. For planar and mildly curved geometry, this requires the computational domain have a sufficiently wide sector size to contain several convective cells. For a spherical geometry, a 4π sector and time enough for several events is needed to capture the geometry of all modes. In general the number of turnovers (time), the number of sectors and plumes per

⁹ Meakin & Arnett (2007b) compared five simulations by different authors, all of whom asserted that MLT gave a fairly reasonable representation of their numerical results, but specific values of ℓ and α varied with the case and code considered.

sector (space) are issues to consider.

4.2. The four-fifths law

An interesting limiting case is Kolmogorov’s “four-fifths law” for homogeneous isotropic turbulence. In our notation,

$$v^3 = -\frac{4}{5}\epsilon_K \Delta r_{cz}, \quad (12)$$

(see Frisch (1995) §6.2). The only spatial scale is the depth of the convection zone Δr_{cz} , so this is for planar geometry, with no curvature. The turbulence is homogeneous and isotropic, on average, over a slab of this depth.

Frisch called Kolmogorov’s 1941 work, of which this law is a major part, “one of the very few exact and nontrivial results in the field.” Thus, using Eq. 3, the ratio of dissipation length to size of the turbulent region is

$$\ell_d/\Delta r_{cz} = 5/4 = 1.25, \quad (13)$$

which is an *analytic* result. Shell burning of O+O (Meakin & Arnett 2007b) is relatively unstratified ($\Delta r_{cz} \lesssim 2H_P$) with modest curvature ($r_{\text{inner}} \not\ll r_{\text{outer}}$). Cristini, et al. (2017) show that the plane parallel approximation is reasonable for the C+C shell. Consequently it is appropriate to compare the *numerical values* for dissipation lengths for O+O and C+C shell simulations to Eq. 13. From Eq. 11, this is an estimate of a “mixing length”, which here is not an adjustable parameter.

4.3. The O+O shell

Using the simulations of Meakin & Arnett (2007b), Arnett, Meakin & Young (2009) found the mass contained in the convection zone to be $M_{cz} \sim 1.84 \times 10^{33}$ g and the total kinetic energy $\int \rho E_K dV \sim 8.61 \times 10^{46}$ ergs, so that the rms velocity was $v_{\text{rms}} = (2E_K/M_{cz})^{1/2} \sim 0.966 \times 10^7$ cm/s. Fig. 2 (right panel) in Arnett, Meakin & Young (2009) suggests that the numerical sub-grid dissipation

from the turbulent cascade is fairly well approximated, on average, through most of the convection zone by the local value of $\epsilon_K = v_{\text{rms}}^3/\ell$. Fitting the integral of the inferred dissipation

$$\int_{cz} \epsilon_K \rho dV = M_{cz} v_{\text{rms}}^3 / \ell_d \quad (14)$$

to the simulation implied $\ell_d \sim 3.6 \times 10^8$ cm at the particular time chosen. A time average of the integral may be constructed for the data (“the hill”) in Fig. 1 and 2.

The oxygen burning simulation begins with an episode of entrainment of ^{20}Ne into the ^{16}O shell, giving two steady-state burning zones in the same convective shell, something never seen in 1D simulations (Mocák, et al. 2018). The oxygen burning shells were done with the PROMPI code and subjected to RA-ILES analysis. Arnett, et al. (2015) discuss the highest resolution simulation (“Perth”) of the oxygen-burning shell. Table 1 summarizes the oxygen-burning shell results, in order of increasing resolution. Structural variables, such as depth of convection zone Δr_{cz} , and density scale height H_ρ , show insensitivity to zoning. The dissipation length ℓ_d (“mixing-length”) is close to the depth of the convection zone, and agrees with the Kolmogorov value (Eq. 13) as well as could be expected from the fluctuations in TKE over the averaging window. Notice that $\alpha_{\text{MLT}} = \ell_d/H_P \approx 2 \approx \Delta r_{cz}$. The rms velocity v_{rms} and the number of turnover times ($t_{\text{ave}}/t_{\text{to}}$) in the average are shown; the higher resolution runs could not be extended in time so far as the lower ones. We find that at least 4 turnovers are desirable for statistical stability in the estimation of the dissipation length.

Resolution effects are subtle; changing zoning also changes initial conditions (Lorenz 1963), and resets the strange attractor. The amplitude of the variations, averaged over the turnover window, seem consistent with the variation in $\ell_d/\Delta r_{cz}$.

Table 1. Dissipation lengths: O+O shell, $\Delta r_{cz} \sim 2H_P$

stage	zoning depth \times area	Δr_{cz} (cm)	ℓ_d (cm)	$\ell_d/\Delta r_{cz}$	ℓ_d/H_P	v_{rms} (cm/s)	$t_{\text{ave}}/t_{\text{to}}$
O shell ^a	400×100^2	4.0×10^8	3.6×10^8	0.90	1.48	0.97×10^7	4
O shell ^b	192×128^2	4.2×10^8	4.9×10^8	1.16	2.03	1.07×10^7	4
O shell ^b	384×256^2	4.2×10^8	5.5×10^8	1.31	2.27	1.09×10^7	4
O shell ^b	786×512^2	4.2×10^8	4.7×10^8	1.12	1.94	1.09×10^7	2.1
O shell ^c	1536×1024^2	4.2×10^8	< 2

^a Meakin & Arnett (2007b); oxygen burning with ^{20}Ne entrainment.

^b Viallet, et al. (2013); oxygen burning with ^{20}Ne entrainment.

^c Arnett, et al. (2015); oxygen burning with ^{20}Ne entrainment (“Perth”).

With these qualifications, it appears that *numerical simulations for weakly-stratified convective regions agree with Kolmogorov theory for homogeneous, isotropic turbulence*. The estimates of

$$\ell_d/\Delta r_{cz} \rightarrow 0.90, 1.16, 1.31, 1.12 \quad (15)$$

do seem to cluster around 5/4 (Eq. 13), apparently within statistical accuracy. Runs of greater duration at high resolution are needed.

The Kolmogorov result is an analytic one, and independent of our choices of numerical parameters like spatial zoning and time step. This agreement supports our choice of zoning in spacetime, and the validity of our method of RA-ILES.

4.4. The C+C shell

Because of the ingestion of ^{20}Ne during oxygen burning, it is interesting to also examine the carbon burning shell, which has no such in-

Again, runs of greater duration at higher resolution are needed, but there seems to be a clustering around 1.25.

gestion, and evolves more gently. To obtain a homogeneous set of simulations, Cristini, et al. (2017) have examined convection in a simple carbon burning shell, changing only the zoning. Table 2 shows the results for C+C shell burning. The energy generation rate for nuclear burning was uniformly boosted over the entire sequence by a factor of 10^3 for numerical reasons; after the boost the burning is still very slow compared to convective turnover. These results are consistent with the oxygen shell simulations. Again, the boundary dissipation spike (in their Fig. 10) tends to disappear at the highest resolutions, while the sub-grid dissipation is insensitive to zoning (their Fig. 9). The cases with highest spatial resolution have available the fewer turnovers, and lose some statistical accuracy for $\ell_d/\Delta r_{cz}$.

Now we have

$$\ell_d/\Delta r_{cz} \rightarrow 1.21, 1.25, 1.17, \dots, 1.20 \quad (16)$$

Table 2. Dissipation lengths: C+C shell^d, $\Delta r_{cz} \sim 2.6H_P$

stage	zoning depth ³	Δr_{cz} (cm)	ℓ_d (cm)	$\ell_d/\Delta r$	ℓ_d/H_P	v_{rms} (cm/s)	t_{ave}/t_{to}
C shell	128 ³	1.030×10^9	1.81×10^9	1.21	3.27	4.05×10^6	3.99
C shell	256 ³	1.033×10^9	2.42×10^9	1.25	3.23	4.56×10^6	4.37
C shell	512 ³	1.025×10^9	2.38×10^9	1.17	2.99	4.53×10^6	10.6
C shell	768 ³	1.027×10^9	2.64×10^9	4.42×10^6	1.5
C shell	1024 ³	1.009×10^9	2.11×10^9	1.20	3.21	4.11×10^6	2

^dCristini, et al. (2017); carbon burning, pseudo-cartesian grid.

5. HIGHLY-STRATIFIED CONVECTION

Kolmogorov’s four-fifths law (Eq. 12) may not be universal, but as we have seen it does apply to weakly-stratified ($\Delta r_{cz} \lesssim 2H_P$) convective regions. In previous sections we have compared MLT to 3D simulations, of mild stratification and of sufficiently high resolution to be turbulent, and developed a replacement for MLT (see §2) which is appropriate for weakly-stratified convection. Here we summarize of some of the modifications due to strong stratification.

5.1. Symmetry breaking

Strong stratification breaks the up-down symmetry assumed in MLT, so that a strong negative flux of kinetic energy occurs, which is not a part of MLT. This agrees with 3D simulations of strongly stratified atmospheres (Nordlund, Stein, & Asplund 2009; Asplund, Ludwig, Nordlund & Stein 2000), in which such negative luminosity components were discovered by Stein & Nordlund (1989). Meakin & Arnett (2010) showed that this was a feature of strong stratification, not of top versus bottom driving. *MLT ignores the fluxes of turbulent kinetic energy, not because they are small relative to enthalpy fluctuations (they are not;*

see Eq. 11), but because they are assumed to cancel by up-down symmetry (Böhm-Vitense 1958, 1989). This asymmetry increases with increasing stratification; mass conservation requires that fast, dense, narrow downflows must be balanced by slow, less-dense, wide upflows (see §2.1). We conclude that *MLT is flawed in detail for strongly-stratified convection zones—deep surface convection—and precise results for the Sun, or red giants, may be questioned.*

5.2. Boundary conditions

Because stellar convection is a fluid dynamic process, it requires a fluid dynamic boundary condition. If the boundary is thin, as generally assumed in stellar evolution, the four close boundaries in Fig. 3 in (Arnett, et al 2019) are condensed into one, so that we have a surface of discontinuity (§81, Landau & Lifshitz 1959). The three dynamic differential equations generate three conditions (conservation of mass, momentum and energy). The two scalar equations (mass and energy) require two scalar jump conditions. The vector (momentum) equation requires three conditions, one for each spatial component of velocity. Enforcing hydrostatic conditions in the stellar radiative region requires an intervening turbulent boundary layer (Landau & Lifshitz 1959, §44),

contrary to MLT assumptions.

Attempting to construct a boundary condition inside a convective region requires knowing the velocity field, with its intermittency and chaos, as well as the thermodynamic variables, luminosity and composition. This is not feasible at present (see §5, Arnett, et al 2019). A specific worry is the treatment of the convective luminosity, L_{conv} , which is the sum of luminosity due to enthalpy fluctuations and to turbulent velocity fluctuations, $L_{\text{conv}} = L_{\text{enthalpy}} + L_{\text{tke}}$, not just $L_{\text{conv}} = L_{\text{enthalpy}}$, as in MLT.

The success of standard stellar evolution with MLT implies that these changes are not large in general, well within correction by the adjustment of a free parameter (the mixing length, overshoot and semi-convection parameters), but are not necessarily unimportant.

5.3. Red giant simulations

Our basis for discussion of strongly-stratified convection are the red giant simulations of Viallet, et al. (2013) which explore convection in a highly stratified shell (Table 3). The simulations were done with the MUSIC code (Viallet, et al. 2011, 2013), which solves the fluid dynamic conservation laws with implicit time stepping, and provides an indication of what modification high stratification requires. This allows larger time steps in the deep, more hydrostatic regions, at the expense of higher computational cost. Despite the completely different hydrodynamic solver, the simulations could be subjected to RA-ILES analysis.

The red giant models show many features common to the weak stratification results; for example, the turbulent kinetic energy fluctuates strongly; compare (Arnett, et al 2019, Fig. 2) and (Viallet, et al. 2013, Fig. 2). While the upper boundary is affected by the choice of a Newtonian cooling approximation for the stellar atmosphere (see below), the lower boundary quickly relaxes to a turbulent

boundary layer, as seen in the weak stratification simulations (see also Arnett & Moravveji 2017).

The most striking differences caused by increased stratification are: (1) the turbulent kinetic energy flux is nonzero, (2) the acceleration due to pressure dilatation is nonzero, and (3) there is a change in waveforms, tending from rolls to plumes. Also, the dissipation length (“mixing-length”) may vary, and global modes (4π geometry) may become important. The turbulent kinetic flux connects (1) a localized source of turbulence to (2) Kolmogorov dissipation, which spreads to encompass the entire turbulent region (Arnett, Meakin & Young 2009). Highly stratified convection with a localized source of turbulence will have a significant flux of turbulent kinetic energy, unlike weakly stratified convection.

The pioneering simulations (Asplund, Ludwig, Nordlund & Stein 2000) of stellar atmospheres focused on resolving the outer layers, where the observed spectra are formed. Viallet, et al. (2011, 2013) focused instead on the bottom layers¹⁰ of the surface convection zone. A complete picture requires both.

5.3.1. Initial model

The stellar structure code used to construct the initial model is described in Baraffe & El Eid (1991). It uses mixing-length theory (with $\alpha = 1.7$) to treat convection, and the extent of the convective region is based on the Schwarzschild criterion. The structure was integrated from the photosphere down to 20% of the stellar radius, stopping to avoid the nuclear burning region. This initial stratification is used as an input model for the multi-D hydrodynamic code. The model is characterized by a total density stratification $\log(\rho_{\text{bottom}}/\rho_{\text{top}}) \sim 4.4$. The total pressure

¹⁰ In a rotating Sun, this is where the tachocline would develop.

stratification is $\log(P_{\text{bottom}}/P_{\text{top}}) \sim 6.2$, or equivalently 14.3 pressure scale-heights. The convective region extends down to $r \sim 2.3 \times 10^{12}$ cm, nearly half of the star in radius. The surface layers are characterized by a strong superadiabatic stratification; which would be explicitly resolved in stellar atmospheres simulations (Nordlund, Stein, & Asplund 2009; Asplund, Ludwig, Nordlund & Stein 2000). The nuclear burning region is not included in the computational domain, instead a radiative flux corresponding to the stellar luminosity is imposed at the inner boundary. As in Viallet, et al. (2011), a proxy was used for the surface layers. In contrast to the case of stellar atmospheres, the red giant simulations explicitly calculate deep turbulent convection, rather than absorb it into an approximate lower boundary condition. A dynamic lower boundary for the convection zone is included, and below that a non-convective radiative region. The steep gradient at the *top* (stellar atmosphere) is replaced by an approximate boundary condition (Newtonian cooling).

These simulations are appropriate for this problem, having a depth of 7.8 pressure scale heights of turbulence. The initial 1D model had a stratification of 14.3 pressure scale heights, with 4.5 pressure scale heights absorbed into the Newtonian cooling region.

Time steps in the implicit code (Viallet, et al. 2011) are constrained by the fluid velocity (accuracy) rather than sound speed. This makes the code behave like an anelastic code for time steps larger than the local sound travel time (in deep layers), damping sound waves, giving incompressible flow, and allowing the deeper layers to be treated dynamically. This may be considered a complement to the approximation used for 3D simulation of stellar atmospheres, emphasizing the physical effects characteristic of the deeper layers rather than the atmosphere.

5.3.2. A possible weakness

We suspect that there may be a flaw in both the red giant simulations (upper boundary), and the stellar atmospheres (lower boundary). In order to stabilize the numerics, adjustment of the dissipation in stellar atmospheres seems¹¹ to result in laminar flow at the bottom of the computational volume, even though the plasma there should be highly turbulent. This numerical effect smears fast downflows. The error might be related to use of a static—not a dynamic—boundary condition. It seems to have little effect on the stellar spectra predicted, but may affect the deep flows. Helioseismic constraints (Hanasoge et al. 2010, 2012; Hanasoge & Sreenivasan 2014), on convective velocity amplitudes ($< 5\text{-}6 \text{ m s}^{-1}$) at large scales ($> 70\text{Mm} = 7 \times 10^9 \text{ cm} \sim 0.01R_{\odot}$), have prompted serious re-examination of radiation hydrodynamics descriptions for stars. This defines a “convective conundrum” (O’Mara, et al. 2018). Accurate simulation of deeper flows (supergranulation) may also require additional physics not in MLT or 321D, such as rotation and MHD, (Miesch, et al. 2012).

In the red giant simulations, the Newton cooling approximation has a similar effect of smearing fast downflows. The two types of simulation are consistent but wrong in the same sense. To remove the ambiguity, a simulation sufficiently well resolved to show turbulent flow over the whole convection zone, may be required. The red giant simulations have a deficit, relative to reality, of narrow fast downflows at the top, which in stellar atmospheres would already appear in the 4.5 scale heights

¹¹ This appears from a visual comparison to demonstrably turbulent flows (e.g., Meakin & Arnett (2007b)). A quantitative estimate of the numerical Reynolds number for the bottom layers of the stellar atmosphere simulations would be helpful for clarification.

absorbed in the Newtonian cooling boundary. These flaws are real but might be minor.

5.4. Red giant simulations

Despite these issues we proceed to abstract some aspects of strongly stratified convection from the existing simulations.

Table 3. Dissipation lengths: Red Giant, $\Delta r_{cz} \sim 7.8H_P$

stage	zoning depth \times area	Δr_{cz} (cm)	ℓ_d (cm)	$\ell_d/\Delta r$	v_{rms} (cm/s)	$t_{\text{ave}}/t_{\text{to}}$
RG ^b	216×128^2	2.0×10^{12}	7.0×10^{11}	0.350	2.27×10^5	3.3
RG ^b	432×256^2	2.0×10^{12}	7.7×10^{11}	0.385	2.34×10^5	3.3

^bViallet, et al. (2013); red giant.

A striking difference from the weakly-stratified case is the smaller value of dissipation length $\ell_d/\Delta r$ (~ 0.38 rather than ~ 1.2). A shorter dissipation length means more dissipation, and less “efficient” convection (in the sense that turbulent “friction” increases in the red giant simulations). Spherical convergence requires a greater force to act on the rapid descending flow, in order to contain it in the smaller volume. This seems to enhance the complexity of the turbulent cascade (Fig. 4, Viallet, et al. 2013).

Another important change occurs in the flow geometry, which transitions from a roll to a plume. Finally, strong stratification implies a more spherical geometry, so that large wavelength global modes may be important (e.g. Woodward et al. (2015)).

Table 3 summarizes the red giant simulations, to be compared with those in §4 for weak stratification. The lower resolutions shown, relative to Table 1 and 2, reflect the greater computational load of the implicit hydrodynamic solver in the MUSIC code; see discussion in (Meakin & Arnett 2007b; Viallet, et al. 2013; Woodward et al. 2015).

5.4.1. Pressure dilatation

We focus on two striking differences: (1) RA-ILES analysis shows that in deeply stratified convection zones, convection is driven to a significant extent ($\sim 40\%$ in the simulations in Table 3) by “pressure dilatation” ($W_P = \langle p' \nabla \cdot \mathbf{u}' \rangle$), in addition to buoyancy, and (2) the radial flux of turbulent kinetic energy is negative and a significant fraction ($\sim 35\%$) of the enthalpy flux.

If the pressure fluctuations are dominated by turbulent ram pressure, $p' \sim \rho(u'_r)^2$, and the rate of decrease in log density (dilatation) is $(\nabla \cdot \mathbf{u}') = u'_r/H_\rho$, then the work done by pressure dilatation is

$$W_P = \left\langle \frac{p'}{\rho} \nabla \cdot \mathbf{u}' \right\rangle \sim (u'_r)^3/H_\rho \sim f v^3/H_\rho, \quad (17)$$

where $f = \overline{(u'_r)^3}/v^3 \leq 1$ is the average projection factor of the radial velocity cubed to the rms velocity cubed. Viallet, et al. (2013) show that W_P becomes comparable to the dissipation rate if H_ρ approaches ℓ_d (strong stratification), and negligible if $H_\rho \gg \ell_d$ (homogeneous background). The ratio of turbulent ram pressure to local pressure, $\rho u'^2/P$, ranges

from $\sim 2 \times 10^{-3}$ at the bottom, to $\sim 2 \times 10^{-2}$ at the top of the convection zone (Viallet, et al. 2013, Fig. 3 and §4.1.1). Consequently the turbulent pressure acts on the flow to accelerate it downward; i.e., it strengthens the downdraft cycle of a convective roll or plume. The cubic dependence on u'_r causes the fastest motion to dominate, so the tendency of buoyancy to produce fast downdrafts and slow updrafts is strengthened.

5.4.2. Turbulent kinetic energy flux

If strongly-stratified convective turbulence is driven by cooling in a thin layer at the top, and spreads downward through the larger mass of the convection zone (Stein & Nordlund 1989, 1998; Arnett, Meakin & Young 2010), it gives a net negative kinetic energy flux. Because of the large heat content, the total energy flux is still positive, but the luminosity has a more complex dependence on ∇_{rad} than in MLT, involving a new quantity, the luminosity due to turbulent kinetic energy L_{tke} , which is nonzero and negative, and affects the quantitative value of the inferred luminosity in a non-negligible way. This error must be absorbed into the calibration of the mixing length.

More generally, we may approximate the general turbulent kinetic equation by

$$d(v^2/2)/dt = \partial_t(\mathbf{v} \cdot \mathbf{v})/2 + \nabla \cdot \mathbf{F}_K = W_B + W_P - \epsilon_K, \quad (18)$$

where, from Eq. 9, we have the rate of work done by buoyancy,

$$W_B = \mathbf{v} \cdot \mathbf{g} \beta_T \Delta \nabla, \quad (19)$$

and from Eq. 17, the rate of work done by

pressure dilatation,

$$W_P \sim f \overline{v^3} / H_\rho, \quad (20)$$

and using Eq. 3,

$$\epsilon_K = \overline{v^3} / \ell_d. \quad (21)$$

In a steady state with no convective zone growth and small wave flux (Eq. 32, Viallet, et al. 2013),

$$W_B + W_P \sim \epsilon_K, \quad (22)$$

or, removing a common factor of v ,

$$\overline{g \beta_T \Delta \nabla} \sim \overline{v^2(1/\ell_d)} - \overline{v^2(f/H_\rho)}, \quad (23)$$

where the averaging is made explicit. This reduces to Eq. 11 in the weak stratification case ($f \rightarrow 0$).

If $\overline{\Delta \nabla} > 0$, this gives a limit for the effective dissipation length ℓ_{dss} in the strong stratification (finite f) limit,

$$\ell_{\text{dss}}/H_P < H_\rho/(H_P f) = (\Gamma/f) \rightarrow \Gamma, \quad (24)$$

or $\alpha_{\text{dss}} = \ell_{\text{dss}}/H_P = \Gamma$. In MLT, $\alpha = \ell_d/H_P$ has no such limiting behavior, which is due to the introduction of pressure dilatation.

We stress that these simple results require an averaging over fluctuations. Damping lags driving (Meakin & Arnett 2007b; Arnett & Meakin 2011) in the weak stratification case. In the strong stratification case, the simple driving-damping classification becomes driving-transport-damping because damping is larger when the whole region is filled with turbulent flow. This causes W_P , W_B and ϵ_K to track each other, in a cycle of potential energy, kinetic energy, and internal energy maxima (Viallet, et al. 2013, §5), like the strange attractor of Lorenz (1963).

5.5. Calibrations of α_{MLT}

Table 4. Some stellar evolution calibrations of $\alpha_{MLT} = \ell_{MLT}/H_P$

reference to code calibration	α_{MLT}^a	$(\delta_\epsilon)^b$
This paper, interior 3D simulations	$\Gamma \sim 5/3 \sim 1.67$	~ 0
Some stellar evolution calibrations:		
Ekström, et al. (2012)	$1.6467(M \leq 1.25M_\odot)$	~ -0.02
Ekström, et al. (2012)	$1.65 (M > 1.25M_\odot)$	~ -0.02
Bressan, et al. (2012)	1.74	$\sim +0.07$
Maeder (1999)	1.6	~ -0.07
Baraffe & El Eid (1991)	1.7	$\sim +0.03$
Young, et al. (2001)	1.6	~ -0.07
Stellar atmosphere calibrations:		
Ludwig, Freytag, & Steffen (1999)	1.577 to 1.80	-0.1 to +0.13
Trampedach, et al. (2014)	1.648 to 1.767	-0.019 to +0.100
Trampedach & Stein (2011)	1.67 to 2.20	0. to +0.53
Trampedach & Stein (2011) (Sun)	1.76	+0.09
Standard solar model calibrations:		
Vinyoles, et al. (2017)	2.18 ^c	$\sim +0.51$
Vinyoles, et al. (2017)	2.11 ^d	$\sim +0.44$

^aWarning: these calibrated values conflate several aspects of convection; see text.

^bHere $\delta_\epsilon = \alpha_{MLT} - 5/3$ may be taken as a rough measure of the consistency of the stellar models with 3D simulations of turbulent convection; see text.

^cB16-GS98 abundances, standard solar model, see reference.

^dB16-AGSS09met abundances, standard solar model, see reference.

Table 4 shows several calibrations of $\alpha_{MLT} = \ell_{MLT}/H_P$ from stellar evolution. They are in reasonable agreement despite the fact that these fitted values of α_{MLT} conflate several distinct issues. For example, the effects of ignoring (1) levitation, due to convective ram pressure in the background momentum equation ([Stein & Nordlund 1989](#)), (2) the flux of turbulent kinetic energy F_{TKE} , and turbulent heating in the background energy equation ([Porter & Woodward 2000](#); [Viallet, et al. 2013](#)), and (3) entrainment due to turbulence at the boundaries ([Meakin & Arnett 2007b](#)),

all make the stellar models incomplete. In addition there may be errors of application, e.g., related to over-simplified algorithms for overshoot and semi-convection. The calibrations are all essentially tests of surface convection zones; they have strong stratification and $\Gamma \sim 5/3$.

These errors are lumped together, as are errors in composition ([Asplund, et al. 2009](#)), whenever the free parameter α_{MLT} is adjusted. If the models were complete and accurate, the error $\delta_\epsilon \sim \alpha_{MLT} - \Gamma$ would be small in magnitude, so the value of $|\delta_\epsilon|$ may be taken as a

new measure of consistency between the stellar models and 3D simulations of turbulent convection. Despite these issues, $\alpha_{\text{MLT}} \sim \Gamma$, or $\ell_{\text{MLT}} \sim H_\rho$, is a surprisingly good approximation. Many modern calibrations use $\alpha_{\text{MLT}} = 1.7$, which is obviously similar.

Renzini (1987) noted that “...one single value of the free parameter gives a very good fit to stellar radii from the main sequence to the tip of the giant branch...”, so that “MLT is not that bad”. The argument above suggests (1) why this is so, (because MLT mimics the universality of the Kolmogorov cascade), and (2) what the value of that single parameter should be ($\alpha_{\text{MLT}} \sim \Gamma \sim 5/3$), and (3) some possible causes of deviations.

5.5.1. α_{MLT} from the Standard Solar Model

It is notable in Table 4 that the values carefully calibrated from the standard solar model (SSM) (Vinyoles, et al. 2017) seem different from those calibrated from other methods. Is a narrow but precise data set more trustworthy than a broader but less precise one? It depends. In SSM the models are constrained to find an optimum fit to additional data from helio-seismology, and should be preferred, *provided they are complete, in the sense that all important physics is accurately represented*. Otherwise optimization in parameter space will find a false solution set.

The use of MLT in the SSM procedure insures that several features are ignored, which are prominent in 3D simulations. The solar neutrino fluxes seem robust to such variations, being most sensitive to conditions in the deep interior which is not convective. However, it is not clear that such optimization of parameters is insensitive to variations at the bottom boundary of the convection zone, the position of which is an important constraint in the SSM procedure (Basu & Antia 1997).

6. CONCLUSION

We have systematically re-examined the unphysical aspects of MLT in 1D stellar evolution, which were summarized in Renzini (1987), by applying Reynolds-averaging to 3D turbulent implicit large eddy simulations (RA-ILES) of the classical Böhm-Vitense problem (Böhm-Vitense 1958) of stellar convection. The RA-ILES combination is “exact” to the word length of the computer used, and we quantify the resolution errors due to zoning. The evolution of the turbulent kinetic energy is chaotic, involving a few dominant modes. This makes interpretation of time aspects of numerical convergence a challenge, but provides insights into the driving of turbulence and stellar variability. The RA-ILES simulations automatically provide the velocity structure at boundaries, including composition profile, structure of deceleration region, and the basis for prediction of wave generation.

To the extent that the “mixing length” is meaningful, it appears to be essentially the Kolmogorov dissipation length, and may be extracted from the simulations. We extract the sub-grid dissipation from the burning shell simulations for O+O and for C+C, which are weakly-stratified. RA-ILES gives sub-grid and boundary dissipation separately; if zoning is changed a “spike” due to resolution error in the turbulent boundary layer gradually disappears, leaving a “hill” due to sub-grid dissipation, and allows an independent estimate of the Kolmogorov dissipation length. This result for weakly-stratified convection is statistically consistent with the Kolmogorov analytic value for homogeneous isotropic turbulence.

For highly stratified convection there is up-down symmetry breaking, and the development of downward acceleration from pressure dilatation as well as a net downward turbulent kinetic energy flux. *This is totally missing from MLT, so MLT should not be used for accurate simulations of high stratification such as found in the Sun and other examples of sur-*

face zones of stellar convection.

This misapplication may be part of a solution to the solar abundance problem (Asplund, et al. 2009), as well as the difficulty with helioseismic constraints (Hanasoge et. al 2010, 2012; Hanasoge & Sreenivasan 2014) and the “convection conundrum” (O’Mara, et al. 2018).

Finally we derive the dissipation length for strong stratification, $\ell_{\text{dss}}/H_P \sim \Gamma$, and show that it is consistent with many empirical calibrations from stellar evolution, leaving the treatment of turbulent boundary layers and strong stratification as major improvements to be made in current theory of stellar convection.

We thank Dr. Maxime Viallet and Dr. Miro Mocák, whose work was an important foundation for this paper. We thank the Theoretical Astrophysics Program (TAP) at the University of Arizona, and Steward Observatory for support. This work was supported by resources provided by the Pawsey Supercomputing Centre with funding from the Australian Government and the Government of Western Australia. This work used the Extreme Science and Engineering Discovery Environment (XSEDE), which is supported by National Science Foundation grant number OCI-1053575. Some computations in our work made use of ORNL/Kraken and TACC/Stampede.

AC acknowledges partial support from NASA Grant NNX16AB25G. AC acknowledges the use of resources from the National Energy Research Scientific Computing Center (NERSC), which is supported by the Office of Science of the U.S. Department of Energy under Contract No. DEAC0205CH11231.

The authors acknowledge support from EUFP7ERC2012St Grant 306901. RH acknowledges support from the World Premier International Research Centre Initiative (WPI Initiative), MEXT, Japan. This article is based upon work from the ChETEC COST Action (CA16117), supported by COST (European Cooperation in Science and Technology). CG, RH, and CM thank ISSI, Bern, for their support on organising meetings related to the content of this paper. CG acknowledge support from the Swiss National Science Foundation and from the Equal Opportunity Office of the University of Geneva.

This work used the DiRAC@Durham facility managed by the Institute for Computational Cosmology on behalf of the STFC DiRAC HPC Facility (www.dirac.ac.uk). The equipment was funded by BEIS capital funding via STFC capital grants ST/P002293/1 and ST/R002371/1, Durham University and STFC operations grant ST/R000832/1. This work also used the DiRAC Data Centric system at Durham University, operated by the Institute for Computational Cosmology on behalf of the STFC DiRAC HPC Facility. This equipment was funded by BIS National Infrastructure capital grant ST/K00042X/1, STFC capital grants ST/H008519/1 and ST/K00087X/1, STFC DiRAC Operations grant ST/K003267/1 and Durham University. DiRAC is part of the National E Infrastructure. We acknowledge PRACE for awarding us access to resource MareNostrum 4 based in Spain at Barcelona Supercomputing Center. The support of David Vicente and Janko Strassburg from Barcelona Supercomputing Center, Spain, to the technical work is gratefully acknowledged.

REFERENCES

- Acton, F. S., 1970, *Numerical Methods That Work*, Harper International Edition, Harper & Row, New York
- Aerts, C., Chistensen-Dalsgaard, J., & Kurtz, D. W., 2010, *Asteroseismology*, (Berlin: Springer)

- Apsden, A. Nikiforakis, N., Dalziel, S., & Bell, J. B., 2008, *Comm APP. Math. Comp. Sci.*, 3, 103
- Arnett, W. D., 1968, *Nature*, 219, 1344
- Arnett, D., 1996, *Supernovae and Nucleosynthesis*, Princeton University Press, Princeton NJ
- Arnett, W. D., 2015, *IAUS* 307, 459
- Arnett, W. D., Meakin, C., & Young, P. A., 2009, *ApJ*, 690, 1715
- Arnett, W. D. & Meakin, C., 2010, *IAUS*, 265, 106
- Arnett, W. D., Meakin, C., & Young, P. A., 2010, *ApJ*, 710, 1619
- Arnett, W. D., & Meakin, C., 2011, *ApJ*, 741, 33
- Arnett, W. D., & Meakin, C., 2016, *Reports of Prog. Phys.*, 79, 2901
- Arnett, W. D., Meakin, C. A., Viallet, M., Campbell, S. W., Lattanzio, J. C. & Mocák, M., 2015, *ApJ*, 809, 30
- Arnett, W. D., & Moravceji, E., 2017, *ApJ*, 836L, 19
- Arnett, W. D., Meakin, C., Hirschi, R., Georgy, C., Campbell, S., Scott, L., Kaiser, E., 2019, (Paper I), submitted to *MNRAS*
- Asplund, M., Grevesse, N., Sayval, A. J., Scott, P., 2009, *ARA&A*, 47, 481
- Asplund, M, Ludwig, H.-G., Nordlund, Å, Stein, R. F., 2000, *A&A*, 359, 669
- Baraffe, I., & El Eid, M., 1991
- Basu, S. & Antia, H. ., 1997, *MNRAS*287, 189
- Böhm-Vitense, E., 1958, *ZA*, 46, 108
- Böhm-Vitense, E., 1989, *Introduction to Stellar Astrophysics*, Vol. 2, *Stellar Atmospheres*, Cambridge University Press
- Bressan, A., et al., 2010, *MNRAS*, 427, 127B
- Buldgen, G., et al., 2017, *A&A*
- Canuto, V. M. & Mazzitelli, I., 1991, *ApJ*, 370, 295
- Canuto, V. M., Goldman, I., & Mazzitelli, I., *ApJ*, 473, 550
- Canuto, V. M. 2012, *A&A*, 528, A76
- Canuto, V. M. 2012, *A&A*, 528, A77
- Canuto, V. M. 2012, *A&A*, 528, A78
- Canuto, V. M. 2012, *A&A*, 528, A79
- Canuto, V. M. 2012, *A&A*, 528, A80
- Chandrasekhar, S., 1939, *An Introduction to the study of Stellar Structure*, University of Chicago Press, Chicago
- Clayton, D. D., 1968, *Principles of Stellar Evolution and Nucleosynthesis*, McGraw-Hill, New York
- Colella, P., & Woodward, P., 1984, *JChPh*, 54, 174
- Cristini, A., et al., 2017, *MNRAS*, 471, 279
- Cristini, A., et al., 2018, submitted.
- Davidson, P. A., 2001, *An Introduction to Magnetohydrodynamics*, Cambridge University Press
- Davidson, P. A., 2004, *Turbulence*, Oxford University Press
- Drake, R. P., 2006, *High-Energy-Density Physics*, Springer, Berlin
- Drazin, P. G., 2002, *Introduction to Hydrodynamic Stability*, Cambridge University Press, Cambridge
- Ekström, S., et al., 2012, *A&A*, 537, A146
- Eggleton, P., Dearborn, D., & Lattanzio, J., 2008, *ApJ*, 677, 581
- Featherstone, N. A., & Hindman, B. W., 2016, *ApJ*, 830, 15
- Frisch, U., 1995, *Turbulence*, Cambridge University Press, Cambridge
- Gabriel, M., Noels, A., Montalbán, J., Miglio, A., 2014, *A&A*, 569, A63
- Gabriel, M. & Belkacem, K., 2018, *A&A*, submitted
- Gagnier, D. & Garaud, P., 2018, submitted
- Garaud, p., Gagnier, D., & Verhoeven, J., 2017, *ApJ*, 837, 133
- Gough, D. O., 1968, *AJ*, 72, 799
- Gough, D. O., 1977, in *Problems of stellar convection*, Proc. 38th Colloquium, Nice, France, Aug. 1976, (A78-28526 11-90) Berlin and New York, Springer-Verlag, 1977, p. 15-56
- Grinstein, Magolin, & Rider, 2007, *Implicit Large Eddy Simulations*, Cambridge University Press
- Hansen, C. J., & Kawaler, S., 1994, *Stellar Interiors: Physical Principles, Structure, and Evolution*, 1st. ed., Springer-Verlag, New York
- Hansen, C. J., Kawaler, S., & Trimble 2004, *Stellar Interiors: Physical Principles, Structure, and Evolution*, 2nd. ed., Springer-Verlag, New York
- Hanasoge, S. M., Duvall, T. L., & DeRosa, M. L., 2010, *ApJ*, 712, L98
- Hanasoge, S. M., Duvall, T. L., & Sreenivasan, K. R., 2012, *Proceed. IN. A. S.*, 109, 11928
- Hanasoge, S. M., & Sreenivasan, K. R., 2014, *Solar Physics*, 289, 3403
- Holmes, P., Lumley, J., & Berkooz, G., 1996, *Turbulence, Coherent Structures, Dynamical Systems and Symmetry*, Cambridge University Press
- Jones, S., R. Andrassy, S. Sandalski, A. Davis, P. Woodward and F. Herwig, 2017, *MNRAS*, 465, 2991
- Joyce, M., & Chaboyer, B., 2018, *ApJ*, 856, 10
- Kippenhahn, R. & Weigert, A. 1990, *Stellar Structure and Evolution*, Springer-Verlag
- Kolmogorov, A. N., 1941, *Dokl. Akad. Nauk SSSR*, 30, 299
- Kolmogorov, A. N., 1962, *J. Fluid Mech.*, 13, 82
- Landau, L. D. & Lifshitz, E. M., 1959, *Fluid Mechanics*, Pergamon Press, London.
- Leveque, R. J., 2002, *Finite Volume Methods for Hyperbolic Problems*, Cambridge University Press, Cambridge, UK

- Lighthill, J., 1978, *Waves in Fluids*, Cambridge University Press, Cambridge, UK
- Lorenz, E. N., 1963, *Journal of Atmospheric Sciences*, 20, 130
- Ludwig, H.-G., Fryettag, B., & Steffen, M., 1999, *A&A*, 346, 111
- Maeder, A., 1999, *Physics, Formation and Evolution of Rotating Stars*, Springer, Berlin
- Manneville, P., 2010, *Instabilities, Chaos, and Turbulence*, Imperial College Press, London
- Meakin, C. A., & Arnett, W. D., *ApJ*, 667, 448
- Meakin, C. A., & Arnett, W. D., *Ap&SS*, 328, 22
- Miesch, M., Featherstone, N., Rempel, M., & Trampedach, R., 2012, *ApJ*, 757, 128
- Mocák, M., Meakin, C., Viallet, M., & Arnett, D., 2014, arXiv, 1401.5176
- Mocák, M., Meakin, C., Arnett, D., & Campbell, S., 2018, submitted.
- Montalbán, J., Miglio, A., Noels, A., et al. 2013, *ApJ*, 766, 118
- Nordlund, A., Stein, R., & Asplund, M., 2009, <http://www.livingreviews.org/lrsp-2009-2>
- O'Mara, B., Miesch, M. S., Featherstone, N. A., Agustson, K. C., 2018, arXiv:1603.06107v1, *Advances in Space Research*, submitted
- Orvendahl, R., Calkins, M., Featherstone, N., & Hindman, B., 2018, *ApJ*, submitted
- Parker, E. N., 1979, *Cosmic Magnetic Fields*, Clarendon Press, Oxford
- Pope, S. B., 2000, *Turbulent Flows*, Cambridge University Press, Cambridge, GB
- Porter, D. H. and P. R. Woodward. 2000, *ApJS*127, 159
- Radice, D., Couch, S., & Ott, C., 2015, *Computational Astrophysics and Cosmology*, 2, 7 (arXiv:1501.03169)
- Renzini, A., 1987, *A&A*, 188, 49
- Smith, Nathan, & Arnett, W. D., 2014, *ApJ*, 785, 82
- Stein, R. F., & Nordlund, A., 1989, *ApJ*, 342, 95
- Stein, R. F., & Nordlund, A., 1998, *ApJ*, 499, 914
- Sytine, I. V., Porter, D. H., Woodward, P. R., Hodson, S. W., Winkler, K.-H., *Journal of Computational Physics* 158 (2000), 225
- Tennekes, H., & Lumley, J. L., 1972, *A First Course in Turbulence*, MIT Press, Cambridge MA
- Trampedach, R., & Stein, R. F., *ApJ*, 731, 78
- Trampedach, R., Stein, R. F., Christensen-Dalsgaard, J., Nordlund, A., Asplund, M. 2014, *MNRAS*, Tritton, D. J., *Physical Fluid Dynamics*, 2nd ed., Oxford University Press, Oxford UK
- Turner, J. S. 1973, *Buoyancy Effects in Fluids*, Cambridge University Press, Cambridge, UK
- Tzeferacos, P. et al., 2018, *Nature Communications*, DOI: 10.1038/s41467-018-02953-2
- Unno, W., Osaki, Y., Ando, H., Saio, H., & Shibahashi, H. 1989, *Nonradial Oscillations of Stars* (2nd ed.; Tokyo: Univ. of Tokyo Press)
- Viallet, M., Baraffe, I., & Walder, R., 2011, *A&A*, 531, 86
- Viallet, M., Meakin, C., Arnett, D., Mocák, M., 2013, *ApJ*, 769, 1
- Vinyoles,, N., Serenelli, A., et. al., 2017, *ApJ*, 835, 202
- Vitense, E., 1953, *ZA*, 32, 135
- Warhaft, Z., 2002, *PNAS* 99, 2481
- Woodward, P. R., 2007, in *Implicit Large Eddy Simulations*, ed. F. F. Grinstein, L. G. Margolin, & W. J. Rider, Cambridge University Press, p. 130
- Woodward, Paul R., Herwig, Falk, Lin, Pei-Hung, 2015, *ApJ*, 798, 49
- Young, P. A., Mamajek, E. E., Arnett, D., Liebert, J., *ApJ*556, 230